

Flow visualization of a bubble penetration through porous media in SAGD process using μ SPIV

Shadi Ansari, Reza Sabbagh, Hiran Soltani and David S. Nobes*

University of Alberta, Department of Mechanical Engineering, Edmonton, Canada

*david.nobes@ualberta.ca

Abstract

Steam assisted gravity drainage (SAGD) is an enhanced recovery method used to recover high viscous crude bitumen from oilsand reservoirs. In this process emulsions are generated in the reservoir through the formation of water bubbles due to interfacial phenomena or heat transfer between the two phases. The presence of water bubbles in the produced oil intensifies the effects of the emulsion flow on the pressure drop and the flow through the surrounding porous medium. The aim of this research is to investigate the deformation of a bubble in an oil flow through a 2D porous medium. The deformation of the bubble is visualized using a micro shadowgraph particle image velocimetry (μ SPIV) method. The results are further analyzed to investigate the pressure drop introduced to the continuous phase by the pore in the presence of a deformed bubble.

1 Introduction

In SAGD, one of the most important parameters to optimize the oil production is the pressure drop of the flow through the porous formation of the reservoir (Butler, 1998). The pressure drop is introduced due to the fluid flow which is affected by the presence of emulsions. In an emulsion flow, the generated bubbles migrate as the dispersed phase in a continuous phase of an immiscible fluid. These individual bubbles may have different interactions with each other and with the surrounding medium depending on their size, the geometry of the pore and present interfacial forces (Tan, 2007; Wang, 2006).

A bubble experiences a deformation when it passes through a pore throat as shown in Figure 1. The change in the bubble shape leads to a pressure difference across the pore as part of a phenomenon known as the Jamin effect which was first introduced in 1860 (Benet, 2017; Wright, 1933) and is described as:

$$\Delta P_c = P_2 - P_1 = 2\sigma \left(\frac{1}{R_2} - \frac{1}{R_1} \right) \quad (1)$$

where ΔP_c is capillary pressure, σ is interfacial tension of the bubble and R_1 and R_2 are the radii of the bubble before and after the pore throat, respectively.

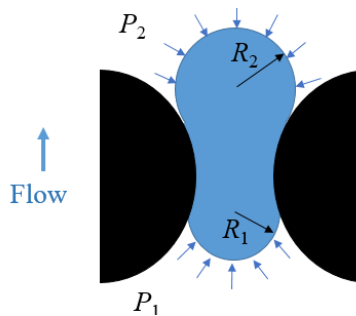


Figure 1: Schematic of a bubble deformation through a pore throat (black is pore throat wall, white is oil and blue is water); after (Benet, 2017)

The capillary pressure resulting from the deformation of the bubble can be used to determine the effect of emulsion flows in porous media. This can be undertaken by measuring the bubble deformation using a visualization technique. An optical diagnostic technique such as particle image velocimetry (PIV) can be

used to measure the motion of the fluid surrounding a bubble. The pressure drop in the flow of the continuous phase caused by the penetration of a bubble, as described in equation (1), can be obtained from the visualization technique.

The pressure of the continuous phase can be calculated by coupling the velocity measurement (from μ SPIV) and the governing equations. Using an integration of the Navier-Stokes' equation for an incompressible fluid (Dabiri, Bose, Gemmill, Colin, & Costello, 2014):

$$\nabla p = -\rho \left(\frac{Du}{Dt} - \nu \nabla^2 u \right) \quad (2)$$

where p is the pressure, ρ is the density of the fluid, u is the velocity, $\frac{D}{Dt}$ is the material derivative, and ν is the kinematic viscosity of the fluid. By integrating the pressure gradient described by equation (2) between any two points (x_1 and x_2) along a streamline, the pressure difference can be calculated as:

$$p_2 - p_1 = \int_{x_1}^{x_2} \nabla p \, dx \quad (3)$$

Based on the equation (2) and equation (3), it can be concluded that the pressure of an inviscid fluid as a continuous phase is only a function of the velocity field, measured in this study using PIV and the properties of the fluid (Dabiri et al., 2014). The result of this study will be useful to form a clear understanding of the pressure distribution at the pore scale and migration of fines through a porous medium in SAGD.

2 Experimental Setup

An imaging experiment was setup to measure the velocity field across a pore using PIV as shown in Figure 2(a). The setup consisted of a camera, a light source and a flow channel. The camera (Phantom v611, Vision Research Inc.) in this experiment can capture the motion of the bubble with frequency up to 5000 Hz. The camera was coupled with an infinity corrected microscopic lens (MPLN with 5 \times magnification) to focus on the interface of the bubbles. The system was illuminated using a high current LED that operated in a continuous mode. The geometry of the flow channel manufactured to represent the pore is shown in Figure 2(b). The flow channel was made of 2 layers - one as the window (optical) access and the other one as a flow channel. The window was made of an acrylic sheet using a laser cutter. The flow channel, on the other hand, was made by 3D printing a clear resin using a commercial printer (Form 2, Formlabs, Inc.). To mimic the geometry of a pore throat, two pillars with a constant aperture size (1 mm) were designed in the flow channel. The flow cell also contained respective inlets and outlets for the continuous and dispersed phases. The continuous phase was seeded using 40 μ m tracer particles that followed the flow. The fluid moved from bottom to top in the flow channel with a constant net flow provided by a syringe pump. The dispersed phase (air) was also injected from the bottom of the channel from a separate source. The bubble of a dispersed phase moved upward due to the presence of the net bulk flow and the density difference between the fluids.

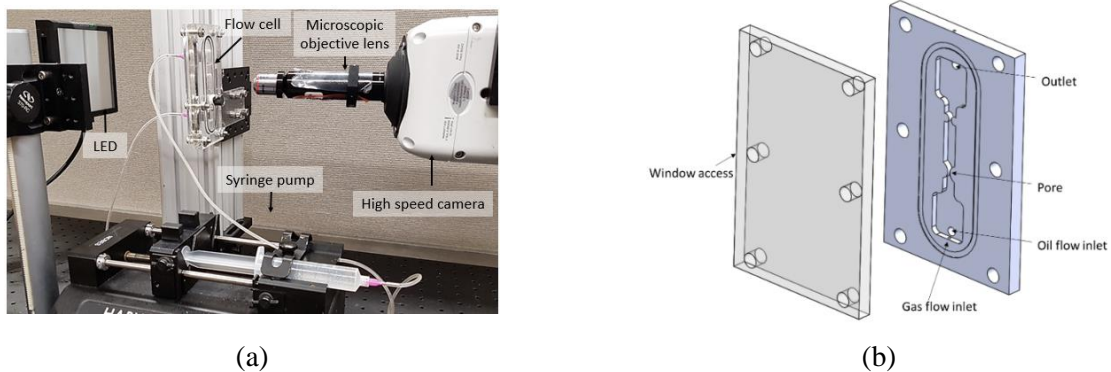


Figure 2: Annotated image of (a) the μ -PIV setup and (b) the flow cell

3 Results

3.1 Bubble motion

The velocity and deformation of a bubble passing through a pore was investigated using μ SPIV. Figure 3(a) to (e) show successive images of the bubble passing through the pore throat. The deformation of the bubble at these locations were modeled by a fitted curved on the front and the back face of the bubble. As shown in Figure 3(a), the bubble had its stable spherical shape before it entered the pore. As the bubble entered the pore, it starts to deform which results in different radii of the front face and the back face of the bubble. As shown in Figure 3(b), when the bubble was located before the pore, the radius of the front face (red circle) was smaller than the back face (green circle). As the bubble moved further into the pore the center of the mass of the bubble aligned with the pore throat, as shown in Figure 3(c), and the back and front face curvatures had the same radii. As the bubble passed the pore throat, its front face curvatures had a greater radius, Figure 3(d) and it gained its spherical shape when it exited the pore throat.

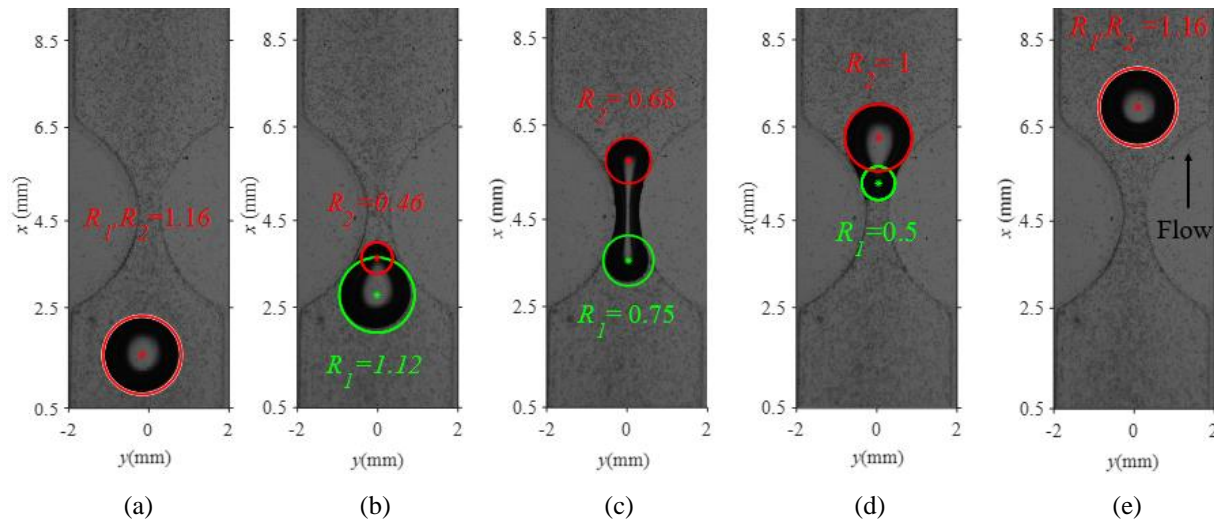


Figure 3: Successive images of a bubble passing through a pore throat (all units are in mm)

The change in the radii of the curvature of the front and back faces of the bubble with respect to the position of its center of area is shown in Figure 4. The pore throat of the channel was located at $x = 4.5$ mm. The curvatures of both faces were constant before the bubble entered the pore, Figure 3(a) for $x < 2$ mm since bubble had its spherical shape. As the bubble entered the pore at $x = 2$ mm the curvatures of both faces decreased. The radius of the front face decreased faster at the entrance of the pore due to the smaller cross-sectional area available for the bubble. The radius of curvature of the front face reached its minimum at $x = 3.5$ mm in Figure 3(b), when the front face was aligned with the pore throat. As the front face passed the pore throat at $x = 4.5$ mm, the radius increased until it became constant at $x = 6.5$ mm which represents the equivalent radius of the bubble seen in Figure 3(e). The back face curvature followed a similar trend as shown in Figure 4. This face, however, had different starting point at $x = 1.75$ mm where the radius of curvature began to decrease since it reached the pore later than the front face. It reached its minimum radius at $x = 5$ mm in Figure 3(d) where it was aligned with the pore throat. At $x = 4.5$ mm, the radii of the front and back faces were comparable as seen in Figure 3(c).

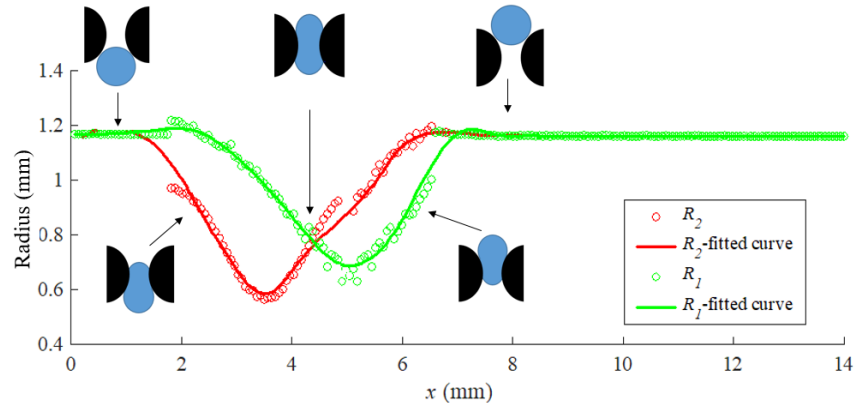


Figure 4: Plots of the change in the front and back face radii of curvatures for a bubble passing through a pore throat

The deformation in the shape of a bubble and the change in the available cross-sectional area resulted in the change in the velocity of the bubble through the pore. In order to study the effect of the deformation, the velocity of the continuous phase and bubble (front face, back face, and the center of area) were compared as shown in Figure 5. The velocities for all cases were normalized by their respective initial velocities to have a better comparison of the change in velocity. It can be seen that the velocity of the bubble center of area and the continuous phase were constant before the pore for $x < 2$ mm since the cross sectional area of the channel was constant. The velocities of the fluids increased in both single- and multi-phase flow scenarios as the bubble enter the pore throat for $x > 2$ mm. They reached their maximum velocity at the pore throat $x = 4.5$ mm and the velocity decreased at locations past the pore and reached the respective initial values farther downstream of the pore for $x > 6.5$ mm.

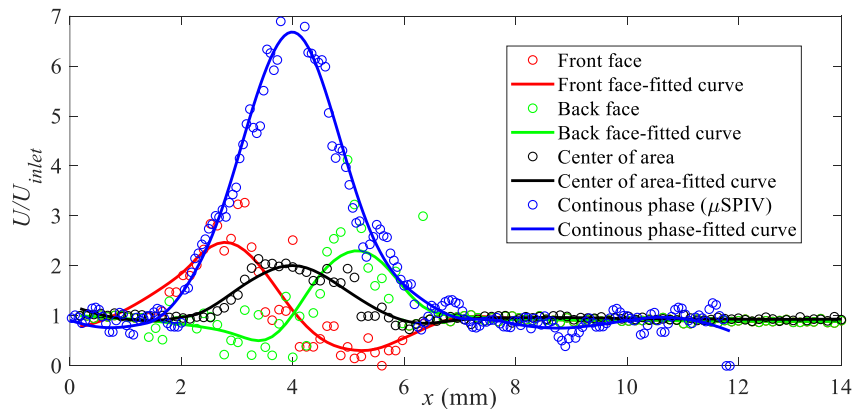


Figure 5: Plot showing the change in the velocities at the front, back, and the center of area of the bubble

As shown in Figure 5, the velocities of the front face and the back face had different trends in comparison with the bubble center of area and the continuous phase velocities. The change in the front face velocity of the bubble started before the bubble entered the pore. It moved faster than the continuous phase as it entered the pore at $x = 2$ mm due to the decrease in cross-sectional area and it reached its maximum velocity when the front face of the bubble was at the pore throat at $x = 3$ mm. After the front face passed the pore, it decelerated to a minimum value at $x = 5$ mm where the back face was aligned with the pore. The velocity of the front face increased to the initial velocity of the bubble as the bubble gained its spherical shape at $x = 6.5$ mm. The velocity of the back face had the opposite trend of the front face. This face had the maximum velocity as the bubble exited the pore at $x = 5.5$ mm. Both front and back faces reached the same velocities at $x = 4.5$ mm where the center of area of the bubble and the pore throat were aligned and they had the same curvature. The continuous phase and the center of area also had the maximum velocity at this point.

3.2 pressure drop

As shown in Figure 5, the continuous phase accelerated more than the bubble in the pore throat. The difference in the change in their velocities resulted from the Jamin effect due to the prevalence of multi-phase flow phenomenon. This phenomenon results in a higher pressure drop in the flow of the continuous phase. The excess pressure difference introduced in the bubble is proportional to the change in the curvature of the front and back face as shown in equation (1) which can be applied under the assumption of constant surface properties for the pore. A representation of the change in the pressure, $\Delta P_c/2\sigma$ at the back and front faces of the bubble is shown in Figure 6. The bubble had a uniform pressure around it before entering the pore as evident by its spherical shape. As it moved closer to the pore, the pressure of the front phase became lower than the pressure of the back face ($\Delta P_c > 0$). This resulted in the deceleration of the bubble movement. The pressure at the front and back faces became equal when the center of area was aligned with the pore ($\Delta P_c = 0$). The pressure of the front face became higher than the back face as the drop passed the pore.

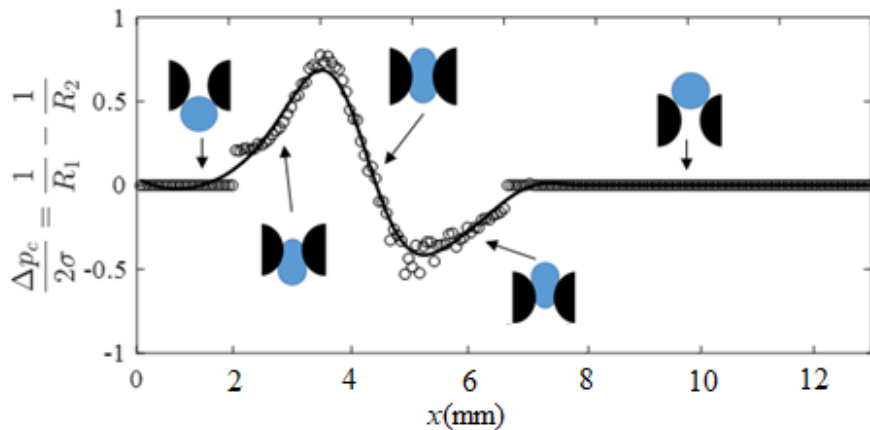


Figure 6: Graph of the change in the radius of the curvature before and after the pore throat

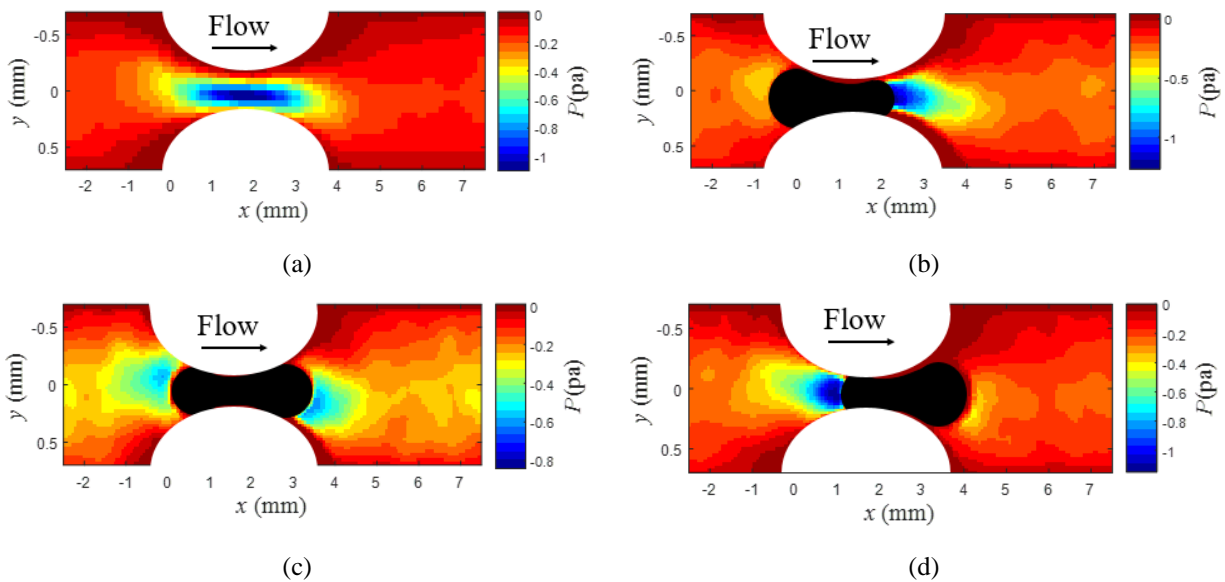


Figure 7: Pressure distribution of the continuous phase (a) without the bubble, (a) bubble entering the pore (b) bubble at the center of the pore and (d) bubble exiting the pore (flow is left to right in all graphs)

The pressure drop generated in the bubble can be also studied by considering the pressure distribution in the continuous phase. The pressure can be determined by an integration of the Navier-Stokes equation for an incompressible fluid along a streamline. The calculated pressure distribution in the continuous field at different locations of the bubble are shown in Figure 7(a) to (d). The pressure map of the continuous phase without the presence of a bubble, Figure 7 (a), shows that the lowest pressure occurs at the center of the pore throat. The velocity has its maximum value at this location. As the bubble entered the pore, Figure 7(b), the location of the minimum pressure moved towards the exit of the pore which resulted in higher velocity of the front face. The pressures on the two sides of the pore became equal as the center of area of the bubble was aligned with the pore throat, Figure 7 (c). As the bubble exited the pore, Figure 7 (e), the maximum velocity occurred at the back face of the bubble. The results from calculating the pressure field in the continuous phase showed the same trend for the velocity and pressure distributions as those shown in Figure 5 and Figure 6.

4 Conclusion

The velocity and the deformation of a bubble passing through a pore was studied using μ SPIV. The results from the analysis of the bubble deformation indicated that the curvature of the front- and back-faces changed as the bubble moved through the pore. The change in the curvature of the faces caused a variation in the pressure field at different stages of the bubble movement through the pore. This resulted in the difference between the velocities of the continuous phase and the dispersed phase – confirming what is stated in the Jamin effect. The results of this study can be further used to investigate the effects of pore geometry, interfacial properties, and the pressure and velocity distributions of a continuous phase on the overall pressure drop. The migration of fines due to pressure gradient and presence of emulsions can be better understood based on the ultimate findings of this research.

Acknowledgements

The authors gratefully acknowledge financial support from Natural Sciences and Engineering Research Council (NSERC) of Canada, the Alberta Ingenuity Fund, and the Canadian Foundation for Innovation (CFI), and RGL Reservoir Management.

References

- Benet, E. (2017). The porous media's effect on the permeation of elastic (soft) particles. *Journal of Membrane Science*, 535(January), 10–19. <https://doi.org/10.1016/j.memsci.2017.04.014>
- Butler, R. (1998). SAGD comes of age! *Journal of Canadian Petroleum Technology*, 37(7), 9–12. <https://doi.org/10.2118/98-07-DA>
- Dabiri, J. O., Bose, S., Gemmell, B. J., Colin, S. P., & Costello, J. H. (2014). An algorithm to estimate unsteady and quasi-steady pressure fields from velocity field measurements. *Journal of Experimental Biology*, 217(3), 331–336. <https://doi.org/10.1242/jeb.092767>
- Tan, Y. C. (2007). Droplet coalescence by geometrically mediated flow in microfluidic channels. *Microfluidics and Nanofluidics*, 3(4), 495–499. <https://doi.org/10.1007/s10404-006-0136-1>
- Wang, C. (2006). Optical measurement of flow field and concentration field inside a moving nanoliter droplet. *Sensors and Actuators, A: Physical*, 133(2 SPEC. ISS.), 317–322. <https://doi.org/10.1016/j.sna.2006.06.026>
- Wright, R. (1933). Jamin effect in oil production. *Bulletin of the American Association of Petroleum Geologists*, 17(12), 1521–1525.